MOEM

Modern Electronic Materials 2024; 10(2): 115–125
DOI 10.3897/j.moem.10.2.129169

Research Article

$LiMn_{0.8}Fe_{0.2}PO_4$ as a promising cathode material in solid-state lithium batteries: Structural and electrical characterization

Zahraa M. Jaafar[1], Thamir Abdul-Jabbar Jumah[2], Natheer B. Mahmood[2,3]

1 Training and Workshop Center, University of Technology, Box Office 19006, Al-Wehda Neighborhood, Baghdad, Iraq

2 Nano-group for Engineering & Material Science Analysis, Baghdad, Iraq

3 General Directorate of Baghdad Education Karkh2, Ministry of Education, Near Bab Al-Sharqi, Baghdad, Iraq

Corresponding author: Natheer B. Mahmood (natheer.basheer@gmail.com)

Received 6 June 2024 ♦ **Accepted** 28 June 2024 ♦ **Published** 4 July 2024

Citation: Jaafar ZM, Jumah TAJ, Mahmood NB (2024) $LiMn_{0.8}Fe_{0.2}PO_4$ as a promising cathode material in solid-state lithium batteries: Structural and electrical characterization. *Modern Electronic Materials* 10(2): 115–125. https://doi.org/10.3897/j.moem.10.2.129169

Abstract

In this study, the synthesis, structural characterization, and electrical property analysis of $LiMn_{0.8}Fe_{0.2}PO_4$ (LM8F) and its carbon-composite variant (LM8F-10%C) as potential cathode materials for solid-state lithium batteries were reported. Employing high-energy ball milling (HEBM) followed by calcination, LM8F was synthesized using ammonium dihydrogen phosphate, lithium carbonate, manganese(II) acetate tetra-hydrate, and iron(III) phosphate as precursors. The introduction of glucose as a carbon source aimed at the formation of a carbon-coated composite to enhance the electrical conductivity of the material. Structural and morphological characteristics of the synthesized materials were elucidated through X-ray diffraction (XRD), Fourier transform infrared spectroscopy (FTIR), and field emission scanning electron microscopy (FeSEM). The XRD results confirmed the olivine and orthorhombic structure of the synthesized material, highlighting its suitability for use as a cathode in solid-state lithium batteries. Electrical properties were assessed using an LCR meter to examine the impact of carbon coating on electrochemical performance. The findings demonstrated that the inclusion of carbon significantly improved the electrical conductivity, potentially leading to enhanced battery performance. This work contributes to the development of high-performance cathode materials for solid-state lithium batteries, paving the way for future advancements in energy storage technologies.

Keywords

lithium manganese iron phosphate ($LiMn_{0.8}Fe_{0.2}PO_4$), high-energy ball milling (HEBM), carbon composite cathode materials, solid-state lithium batteries

1. Introduction

The quest for advanced cathode materials that can fulfill the growing demands of solid-state lithium batteries has intensified in recent years [1–3]. Among various candidates, olivine-structured phosphates, particularly lithium iron phosphate ($LiFePO_4$), have attracted significant attention due to their excellent thermal stability, safety, and cycle life. However, the intrinsic limitations of these materials, such as low electronic conductivity and poor

ion diffusion rates, have prompted researchers to explore doped variants and composites to enhance their performance [4–9]. In this context, lithium manganese iron phosphate ($LiMn_{0.8}Fe_{0.2}PO_4$, LM8F) emerges as a promising material by combining the high capacity of manganese-based cathodes with the structural stability and safety of iron phosphates [10–15]. The partial substitution of Mn for Fe in the olivine structure has been reported to improve electronic conductivity and lithium-ion diffusion, as well as to provide a more favorable voltage plateau for battery operation [16–21] The incorporation of carbon into cathode materials has been widely recognized as an effective strategy to address the conductivity limitations [4, 5, 22–25]. Carbon-coated and carbon-composite cathode materials have demonstrated significantly enhanced electronic conductivity and, consequently, improved electrochemical performance [23, 26–29]. This approach has been particularly beneficial for phosphate-based materials, where the insulating nature of the phosphate groups hinders electron transport [10, 30, 31]. High-energy ball milling (HEBM) presents a versatile and cost-effective method for the synthesis of composite materials, offering the advantages of simplicity, scalability, and the ability to achieve a uniform distribution of dopants and conductive additives [30, 32–36] Previous studies have successfully employed HEBM to synthesize various cathode materials for lithium-ion batteries, highlighting its potential for the production of LM8F and its carbon-composite variants. Alternative methods for synthesizing $LiMn_{0.8}Fe_{0.2}PO_4$, such as the hydrothermal method or sol-gel method, are available. However, high-energy ball milling is simpler and more cost-effective compared to these techniques. This work aims to explore the synthesis of LM8F and its carbon-composite (LM8F-10%C) through a high-energy ball milling process, followed by a detailed investigation of their structural, morphological, and electrical properties. The synthesis process involves the use of ammonium dihydrogen phosphate ($NH_4H_2PO_4$), lithium carbonate (Li_2CO_3), manganese(II) acetate tetrahydrate ($Mn(CH_3COO)_2 \cdot 4H_2O$), and iron(III) phosphate ($FePO_4$) as precursors, with glucose serving as the carbon source for the composite material. The impact of carbon coating on the electrical conductivity and thermal stability of LM8F is examined, providing insights into the potential enhancements in electrochemical performance offered by this approach. Through this study, the characteristics of LM8F and LM8F-10%C are elucidated, underlining their viability as cathode materials for next-generation solid-state lithium batteries.

2. Materials and methods

2.1. Materials preparation

$LiMn_{0.8}Fe_{0.2}PO_4$ (LM8F) was synthesized using HEBM on MiniMill II apparatus. The starting materials included ammonium dihydrogen phosphate ($NH_4H_2PO_4$) as the phosphate source, lithium carbonate (Li_2CO_3) as the lithium source, manganese(II) acetate tetra-hydrate ($Mn(CH_3COO)_2 \cdot 4H_2O$), and iron(III) phosphate ($FePO_4$) as the sources of manganese and iron, respectively. Glucose powder ($C_6H_{12}O_6$) was employed as a carbon source for creating a composite material. The stoichiometric calculation for obtaining LM8F was guided by the reaction equation:

$$Li_2CO_2 + 1.6\ Mn(CH_3COO)_2 \cdot 4H_2O +$$

$$1.6NH_3H_2PO_4 + 0.4FePO_4 \rightarrow 2LiMn_{0.8}Fe_{0.2}PO_4 +$$

$$nH_2O + 4CO_2 + 1.6NH_3.$$

2.2. High-energy ball milling process

The mixture was subjected to high-energy ball milling at 270 rpm for 8 h. Subsequently, a portion of the milled powder was analyzed using a Q-600 Thermo-gravimetric analyzer for TGA–DSC–DTA analysis. This analysis aimed to investigate the reaction mechanism and structural stability under temperature effects. The conditions included a 60 ml/min argon gas flow and a heating rate of 20 °C/min over a temperature range from 23 °C to 1000 °C.

2.3. Calcination

Post-milling, the powder was calcined at 700°C for 3 h under a nitrogen atmosphere to prevent iron oxidation.

2.4. Structural characterization

The crystal structure of the calcined powder was studied using X-ray diffraction (XRD) on a panalytical diffractometer operating at 45 kV and 30 mA. The diffraction patterns were collected over a 2θ range of 20° to 80° with a step time of 1 sec. using CuK_α radiation (λ = 0.15406 nm). For molecular property analysis, Fourier transform infrared spectroscopy (FTIR) was conducted using a SHIMADZU instrument, covering a wavenumber spectrum from 400 to 4000 cm^{-1} with a KBr disc method. The morphology and microstructure were examined using a field emission scanning electron microscope (FeSEM).

2.5. Preparation of carbon-composite material

To prepare the carbon-composite version, LM8F-10%C, glucose powder was mixed with the initial materials to achieve a 10% carbon content by weight, aiming for a carbon-coated product. Both the LM8F and LM8F-10%C samples were compacted into cylindrical disks (diameter = 12 mm, thickness = 1 mm) using a uniaxial hydraulic press at 100 kN pressure, and then sintered under N_2 atmosphere at 700 °C for 3 h.

2.6. Electrical property analysis

The electrical properties of the sintered samples were analyzed to assess the impact of carbon coating on LM8F's electrical performance. An LCR meter (WK4310) with a frequency range of 20 Hz to 100 KHz was employed. Both Bode and Nyquist plots were utilized to distinguish between the carbon-coated and non-coated samples. The temperature's effect on electrical impedance and conductivity was also studied using the same LCR meter, providing insights into the material's behavior under varying thermal conditions.

This comprehensive experimental approach enabled a detailed exploration of LM8F's suitability as a cathode material for solid-state lithium batteries, focusing on structural, morphological, and electrical characteristics, with a particular emphasis on the enhancements provided by carbon coating.

3. Results and discussion

3.1. Thermal analysis of precursor

The comprehensive examination of the thermal behavior of solid solution LM8F precursors during the calcination process provides critical insights into their stability and decomposition patterns. These insights are essential for refining their synthesis for application as cathode materials in lithium-ion batteries. Figures 1*a* and 1*b* effectively illustrate these thermal properties, presenting the thermogravimetric analysis (TGA) and the derivative thermogravimetry (DTG) curves. The TGA curve elucidates the weight changes experienced by the LM8F precursors as a function of temperature, laying the groundwork for understanding their thermal stability. The DTG curve, derived from the TGA data, further refines this understanding by identifying the exact temperatures at which these weight changes occur, offering a more detailed view of the precursor's calcination behavior.

This dual analytical approach not only increases the precision of the thermal characterization but also streamlines the interpretation of the calcination dynamics of LM8F precursors. The DTG curve is especially beneficial as it clearly marks significant thermal events, such as decomposition or phase transitions, by showcasing peaks that correspond to rates of weight loss. This method enables a deeper investigation into the thermal stability and decomposition pathways of the precursors, pivotal for comprehending the formation mechanisms of the LM8F phase. Moreover, by linking these thermal events to specific temperatures, researchers can tailor the calcination process to achieve complete conversion of precursors into the desired cathode material, thereby reducing the formation of undesirable by-products. The analysis of LM8F precursors' thermal behavior is more than a mere step in material synthesis; it is a gateway to understanding the complex chemical reactions that occur during heat treatment. As we delve into the results and discussion sections, we will explore the impact of these thermal characteristics on the final material properties of LM8F, such as crystal structure, purity, and electrochemical performance. Understanding the thermal decomposition and stability of these materials is fundamental to developing more efficient and durable synthesis methods, potentially leading to cathode materials that enhance the performance of lithium-ion batteries. The thermogravimetric analysis is depicted in Fig. 1*a*. outlines four distinct intervals of mass reduction throughout the heating protocol for the LM8F precursors. The initial stage, occurring between 50 and 90 °C, results in a 3.66% loss in mass, primarily due to the evaporation of water molecules adsorbed on the surface and within manganese acetate [32, 37], leading to its anhydrous form, and possibly the evaporation of residual ethanol. The second interval, between 130 and 160 °C, shows a 9% decrease in mass. In the third interval, from 175 to 209 °C, there's a 4% reduction in mass.

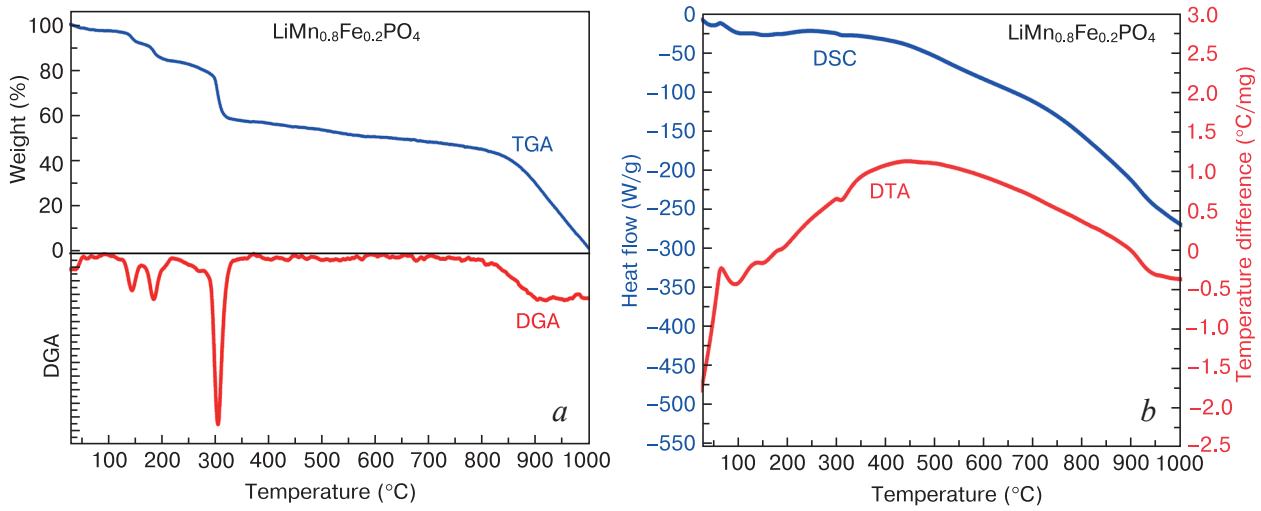

Figure 1. (*a*) Thermogravimetric analysis of LM8F precursor; (*b*) differential thermal analysis and differential scanning calorimetry curves for LM8F precursors

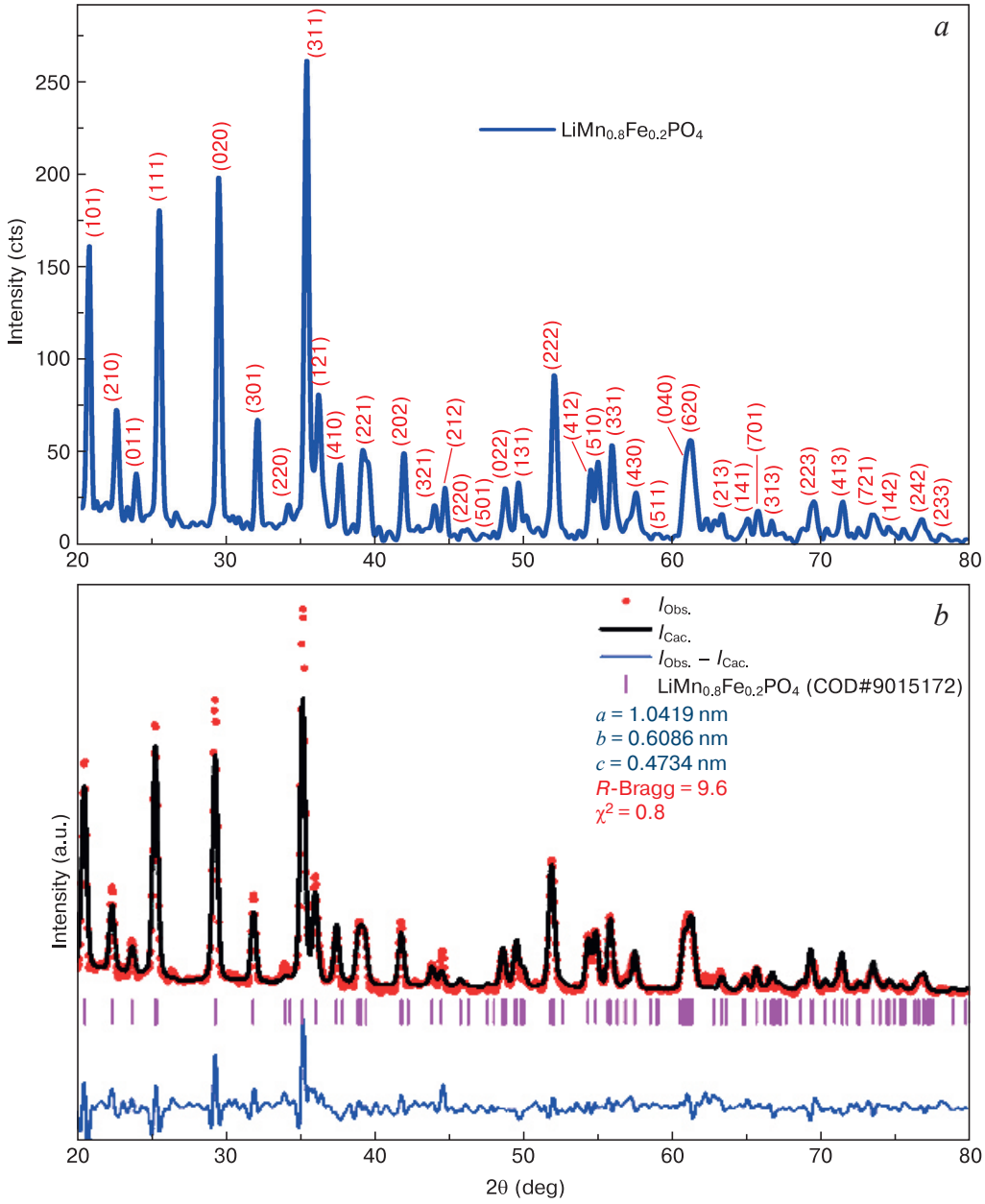

Figure 2. (*a*) XRD pattern of LM8F sample and (*b*) Rietveld refinement of LM8F sample

The final and most significant interval, ranging from 291 to 340 °C, exhibits a 18% mass loss, indicative of the loss of crystalline water, decomposition of manganese acetate, degradation of organic phosphonates, and breakdown of carbonates, respectively. The thermogravimetric curve's plateau between 400 and 750 °C suggests the end of phase transitions and likely marks the start of the LM8F crystallization process around 420 °C. Complementing the TGA data, Fig. 1*b* presents the differential thermal analysis (DTA) and differential scanning calorimetry (DSC) curves for LM8F precursors. An initial exothermic peak at 91 °C on the DTA curve corresponds to desorption processes. Additionally, a series of exothermic peaks from 151 to 320 °C on the DTA curve, closely paralleled by the DSC curve within the same temperature range, indicates the stages of decomposition as identified by the TGA. An endothermic peak at 420 °C on the DTA curve is associated with the crystallization phase of the sample, in line with the thermogravimetric analysis's indication of crystallization initiation at a similar temperature.

3.2. Synthesis and structural characterization

The successful synthesis of LM8F was confirmed through a series of structural and morphological analyses. X-ray diffraction patterns shown in Fig. 2*a* revealed the characteristic peaks corresponding to the olivine and orthorhombic structure with space group *Pnma* of LM8F, in alignment with the standard COD#9015172 [38–40]. This phase purity indicates a successful synthesis process, with no detectable secondary phases, suggesting that the HEBM followed by calcination under a nitrogen

Table 1. Crystallite size for LM8F

2θ (deg)	*d* (nm)	I/I_0	FWHM total	FWHM instr.	FWHM sample	Crystallite size (nm)
20.585	0.43112	520.2	0.3	0.09	0.21	40.19
22.435	0.39597	214.1	0.4	0.09	0.31	27.31
23.735	0.37457	84.1	0.3	0.09	0.21	40.41
25.285	0.35195	662.5	0.4	0.09	0.31	27.45
29.335	0.30421	741.3	0.4	0.09	0.31	27.69
31.935	0.28001	224.6	0.4	0.1227	0.2773	31.15
34.035	0.26320	52.5	0.5	0.1372	0.3628	33.94
35.235	0.25451	1000	0.4	0.1157	0.2843	30.65
36.085	0.24870	256.6	0.4	0.1014	0.2986	29.25
37.535	0.23942	132.5	0.4	0.0804	0.3196	27.44
39.085	0.23028	176.4	0.4	0.0861	0.3139	28.07
41.835	0.21575	166.5	0.3	0.0951	0.2049	43.39
43.885	0.2.0614	60.6	0.4	0.0992	0.3008	29.76
44.585	0.2.0306	89	0.4	0.0978	0.3022	29.7
48.685	0.18688	97.3	0.4	0.0904	0.3096	29.44
49.535	0.18387	105.5	0.4	0.09	0.31	29.5
50.085	0.18198	32.1	0.4	0.09	0.31	29.57
51.985	0.17577	344.7	0.5	0.09	0.41	32.53
54.935	0.16700	155.6	0.4	0.09	0.31	30.19
55.885	0.16439	190.4	0.4	0.09	0.31	30.32
57.485	0.16019	97.1	0.5	0.09	0.41	23.1
61.135	0.15147	217.7	0.7	0.09	0.61	25.81
63.285	0.14683	50.5	0.4	0.09	0.31	31.47
65.035	0.14330	43.3	0.4	0.09	0.31	31.77
65.735	0.14194	58.9	0.4	0.09	0.31	31.89
66.635	0.14024	35.2	0.4	0.09	0.31	32.06
69.485	0.13517	83.3	0.5	0.0948	0.4052	24.94
71.435	0.13195	80.8	0.5	0.0993	0.4007	25.53
73.485	0.12877	57.7	0.6	0.1	0.5	22.73
76.785	0.12403	48.6	0.6	0.1	0.5	23.19
average =			34.45 nm			

atmosphere was effective in achieving the desired stoichiometry and crystallinity.

In the subsequent stage of phase determination, the XRD pattern of the calcined LM8F powder was subjected to Rietveld refinement, with the procedural intricacies depicted in Fig. 2*b*. Utilizing the FullProf Suite for this refinement revealed a remarkable alignment between the experimentally obtained pattern and the theoretical model generated through the Rietveld refinement process. The lattice parameters for the LM8F powder were meticulously refined to a = 1.0419 nm, b = 0.6086 nm, and c = 0.4734 nm, showing a close resemblance to the values documented in the Crystallography Open Database COD#9015172 [38, 39], which are recorded as a = 1.04145 nm, b = 0.60795 nm, and c = 0.47403 nm. The refinement process culminated successfully with a goodness-of-fit value (χ^2) of 0.8, and an *R*-Bragg factor of 9.6, verifying the accuracy of the analysis. Additionally, the average crystallite size of the LM8F powder, determined to be 34.45 nm using the Scherrer equation, is detailed in Table 1. This rigorous analysis highlights not only the precision in aligning the observed data with the established crystalline structure but also confirms the high purity of the synthesized powder.

Fourier transform infrared spectroscopy analysis further corroborated the structural integrity of the synthesized materials. Peaks observed in the FTIR spectra were consistent with the vibrational modes of PO_4^{-3} groups,

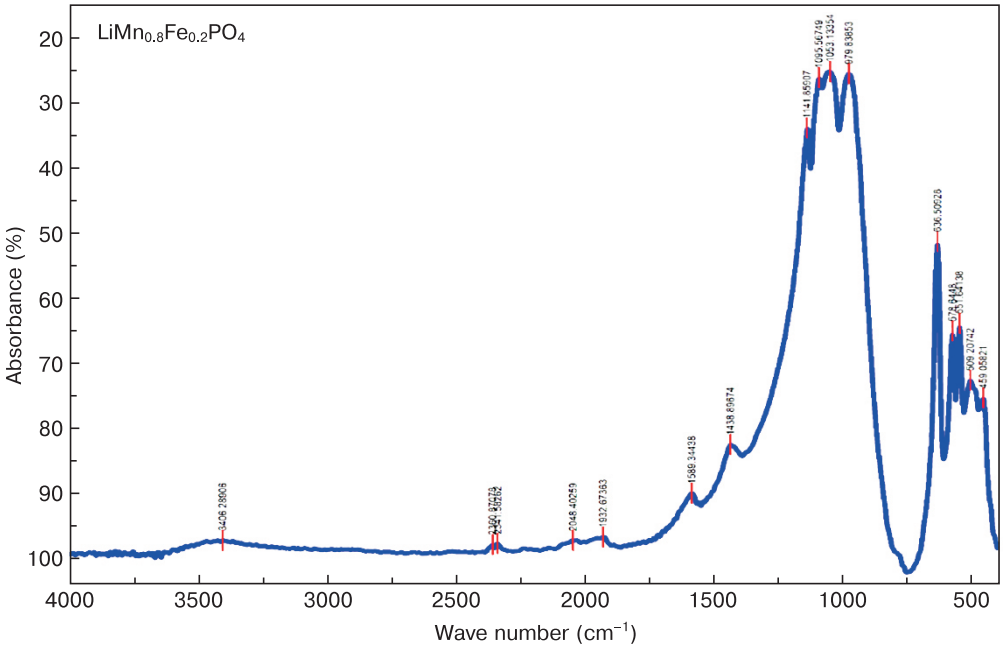

Figure. 3. FTIR spectrum for LM8F

characteristic of the olivine phosphate structure. The absence of bands associated with impurities further confirmed the purity of the synthesized material. Figure 3 showcases the FTIR analysis of the LM8F powder after undergoing calcination. The spectrum identifies specific vibrational modes across two major frequency ranges: from 400 to 560 cm^{-1} and 1000 to 1200 cm^{-1}. The vibrations detected between 459 and 636 cm^{-1} are attributed to the bending movements (including both asymmetric and symmetric) of the O–P–O bonds within the phosphate $[PO_4]^{-3}$ groups. The presence of peaks within the 979 to 1141 cm^{-1} range signals the stretching vibrations of the P–O bonds in the phosphate groups, encompassing both symmetric and asymmetric types. The spectrum also reveals absorption bands spanning from 1438 to 1589 cm^{-1}, which correspond to the bending vibrations of water molecules [41, 42]. Additionally, fainter peaks observed in the 2341 to 2360 cm^{-1} region are associated with the asymmetric stretching of C–O bonds in CO_2 molecules, peak at 2048 cm^{-1} related to O_2, and finally peak at 3406.28 cm^{-1} related to Asymmetric Stretch OH^{-1}. These FTIR spectral features for the LM8F powder are meticulously cataloged in Table 2. Discussing these results, the FTIR spectral analysis provides profound insights into the chemical structure of the calcined LM8F powder. The identification of vibrational modes related to O–P–O and P–O bonds within the phosphate groups validates the presence of the phosphate framework in the LM8F structure, which is fundamental for its application as a cathode material in lithium-ion batteries. The detection of water molecule vibrations suggests some level of hydration post-calcination, which could influence the electrochemical properties of the material. The observed CO_2-related peaks may be indicative of atmospheric CO_2 absorption onto the powder's surface, highlighting the reactive nature of the calcined material. These spectral characteristics not only affirm the successful synthesis of the LM8F powder but also underscore the importance of controlling the calcination environment to minimize unwanted chemical interactions.

Figure 4*a* displays an FE-SEM (*Field Emission Scanning Electron Microscopy*) image of the calcined LM8F powder, showcasing agglomerated semi-spherical particles. The image vividly demonstrates that these particles tend to cluster together, forming agglomerates

Table 2. FTIR vibrational modes for $LiMn_{0.8}Fe_{0.2}PO_4$

Index	Vibration	Peak (cm^{-1})
1	Asymm. Bend PO_4^{-3} (V_2)	459.05821
2		509.20742
3		551.64138
4		578.64480
5	Symm. Bend PO_4^{-3} (V_2)	636.50928
6	Symm. Stretch PO_4^{-3} (V_1)	979.83853
7	Asymm. Stretch PO_4^{-3} (V_3) B_{3g}	1053.13354
8	Asymm. Stretch PO_4^{-3} (V_3) B_{2g}	1095.56749
9	Symm. Stretch PO_4^{-3} (V_3)	1141.85907
10	Symm. Bend H_2O	1438.89674
11		1589.34438
12	O_2 (O–O stretching)	1932.67363
13		2048.40259
14	Doublet CO_2 (C–O asymmetric stretching)	2341.58262
15		2360.87078
16	Asymm. Stretch OH^{-1}	3406.28906

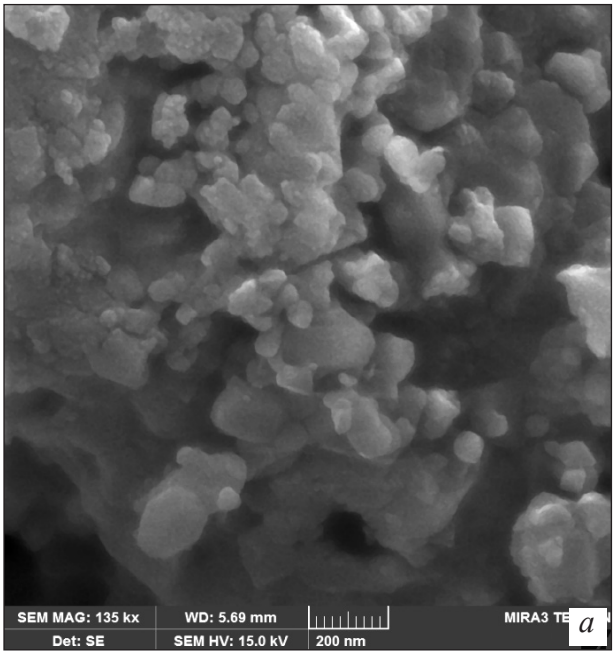

Figure 4. (*a*) FeSEM image for LM8F and (*b*) particle size distribution for LM8F

with a semi-sphere shape. Within these agglomerates, several structural imperfections, including voids and dislocations, are clearly visible, suggesting a complex microstructure. Figure 4*b* then presents the particle size distribution of the calcined LM8F powder through a histogram, indicating that the average particle size is approx. 48 nm. Discussing these observations, the FE-SEM analysis of the LM8F powder highlights the semi-spherical morphology and the tendency of the particles to agglomerate. These features are critical in determining the electrochemical performance of the material as a cathode in lithium-ion batteries. Agglomeration can affect the lithium-ion diffusion pathways and, consequently, the rate capability of the battery. The presence of voids and dislocations within the clusters may also impact the material's structural integrity and its ability to maintain consistent electrochemical properties under cycling conditions. However, the relatively small average particle size of 48 nm is advantageous, as it can potentially enhance the surface area available for lithium-ion interaction, thereby improving the material's overall electrochemical performance. This balance between morphology, agglomeration, and particle size is crucial for optimizing the LM8F powder for use in lithium-ion battery cathodes [6, 30, 43].

3.3. Electrical property analysis

Electrical measurements were performed on both LM8F and LM8F-10%C samples to assess the impact of carbon coating as shown in Fig. 5*a*. The results showed a significant enhancement in the electrical conductivity of LM8F-10%C compared to the uncoated LM8F sample. This improvement can be attributed to the carbon coating facilitating electron transport across the material, which

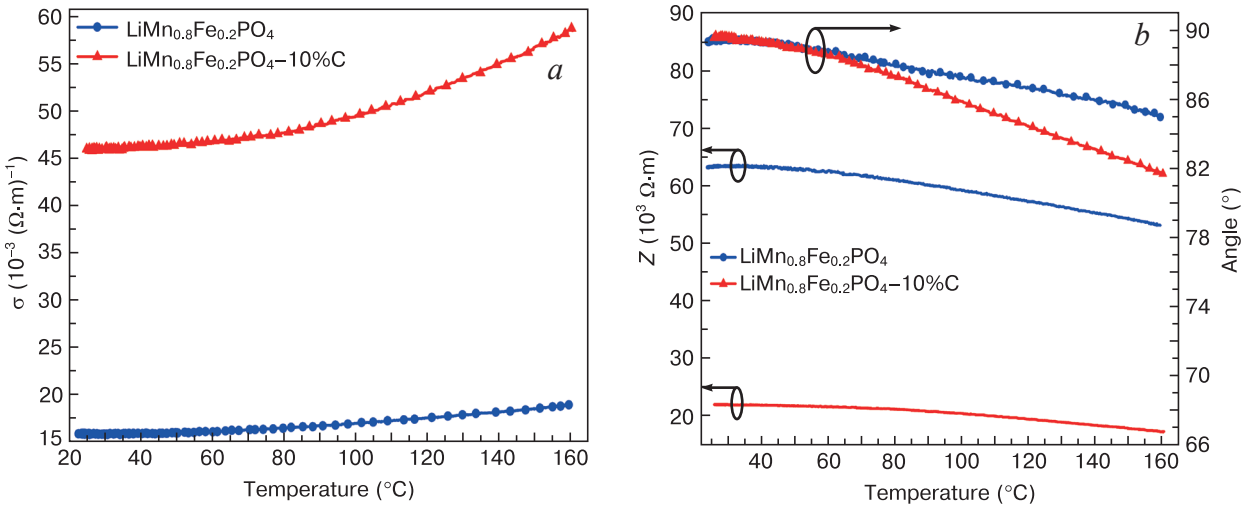

Figure 5. (*a*) Electrical conductivity and (*b*) electrical impedance and phase angle of LM8F and LM8F-10%C varied with temperature

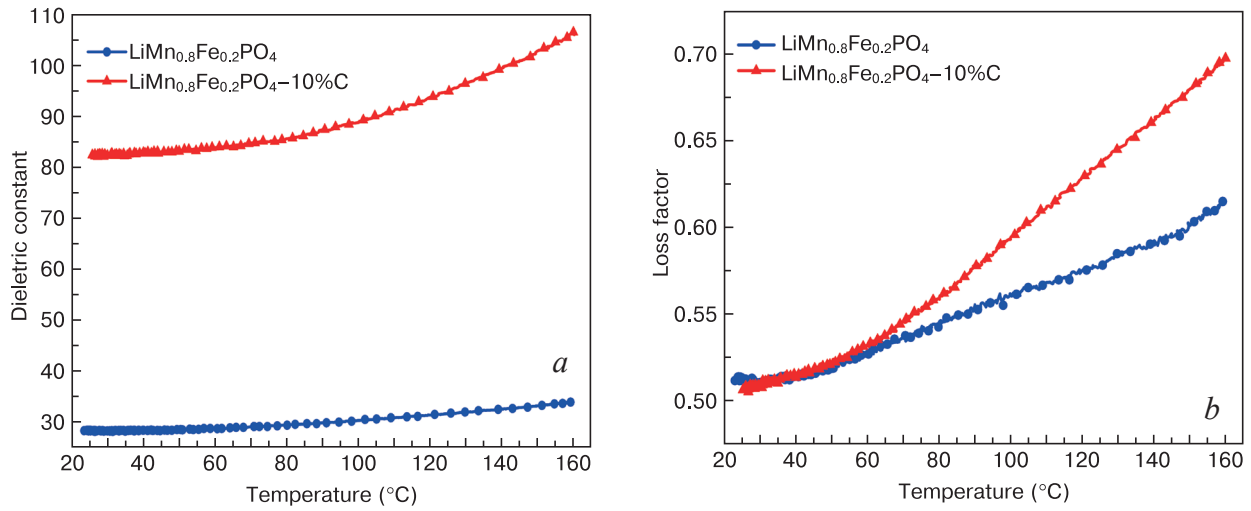

Figure 6. (*a*) Dielectric constant and (*b*) dielectric lose factor of LM8F and LM8F-10%C varied with temperature

is crucial for efficient cathode performance in solid-state lithium batteries.

Temperature-dependent impedance measurements indicated a decrease in resistance with increasing temperature for both samples shown in Fig. 5*b*. However, the LM8F-10%C composite exhibited a more pronounced decrease, suggesting better thermal stability and ion mobility at elevated temperatures. These findings align with the expectation that carbon incorporation should mitigate the intrinsic electronic conductivity limitations of phosphate-based cathode materials.

Figures 6*a* and 6*b* depict the dielectric properties of the solid solution LM8F and LM8F-10%C, respectively. The incorporation of carbon results in a noticeable enhancement of the dielectric constant while concurrently reducing the loss tangent, indicating improved stability with temperature. Specifically, the addition of a carbon coating to LM8F not only elevates the dielectric constant but also diminishes the loss factor. The observed increase in the dielectric constant for LM8F-10%C compared to LM8F can be attributed to the interface polarization at the carbon-material interfaces. Carbon's conductive nature introduces additional polarizable interfaces within the composite, enhancing the material's ability to store electrical energy, reflected in a higher dielectric constant. This interface polarization, known as Maxwell–Wagner–Sillars polarization, is more pronounced in composites containing conductive fillers like carbon, leading to the observed enhancement in dielectric properties. Conversely, the reason behind the greater loss tangent in LM8F-10%C compared to pure LM8F involves the complex interplay between conductivity and dielectric behavior. While the carbon coating improves the dielectric constant due to increased polarization, it also introduces free charge carriers that can contribute to dielectric loss, especially at lower frequencies. These free carriers, moving under the influence of the applied electric field, can lead to increased energy dissipation, manifested as a higher loss tangent. The balance between enhanced dielectric properties and controlled dielectric loss is crucial, as it influences the material's efficacy in applications

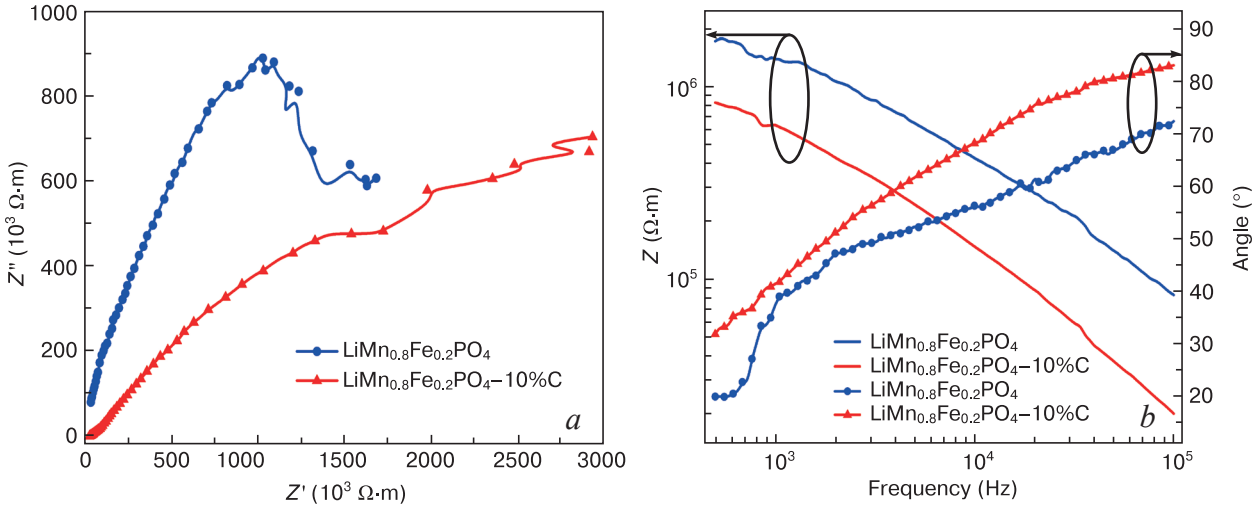

Figure 7. (*a*) Nyquist plot and (*b*) bode plot of LM8F and LM8F-10%C

requiring stable dielectric behavior under varying temperature conditions.

Bode and Nyquist plots further confirmed the superior electrical performance of the carbon-composite material. The Nyquist plots shown in Fig. 7*a* of LM8F-10%C displayed a smaller semicircle in the high-frequency region, indicating a lower charge-transfer resistance compared to LM8F. This observation is consistent with the enhanced conductivity facilitated by the carbon network within the composite material. Bode plot shown in Fig. 7*b* for both LM8F and LM8F-10C shows a capacitive behavior for the impedance with lower impedance for carbon coated sample. The phase angle for LM8F appears near 90° while for LM8F-10%C was below 90° which means an increase in conductance due to carbon coating.

The synthesis strategy employed in this study successfully produced LM8F with a pure olivine and orthorhombic structure, as confirmed by XRD and supported by FTIR and FeSEM analyses. The addition of carbon not only improved the electrical conductivity but also enhanced the thermal stability and ion mobility of the material, as evidenced by temperature-dependent impedance measurements.

4. Conclusion

This study thoroughly examined the thermal behavior, structural features, and electrical properties of $LiMn_{0.8}Fe_{0.2}PO_4$ (LM8F) and its carbon-coated variants for lithium-ion battery cathodes. Through thermogravimetric and differential thermal analyses, we identified critical thermal stability and decomposition patterns, essential for optimizing calcination processes and achieving high-purity cathode materials. X-ray diffraction and Fourier Transform Infrared Spectroscopy confirmed the structural integrity of synthesized LM8F. Morphological analysis highlighted the impact of semi-spherical particle shapes and agglomeration on electrochemical performance, emphasizing the importance of synthesis control. Carbon coating significantly improved LM8F's electrical conductivity, enhancing its potential as a high-performance cathode material. These insights into LM8F's thermal, structural, and electrical aspects advance the development of efficient, durable lithium-ion batteries, contributing to sustainable energy storage solutions.

Acknowledgements

The authors express their profound appreciation to the Nano-Group for Engineering and Material Science Analysis (NEMSA) for their exceptional support and expertise in analyzing the data presented in this study. NEMSA's detailed and expert analysis was crucial in deepening the understanding of our experimental results, significantly elevating the quality and significance of our research. Their contribution was key to refining our interpretations and enhancing the scholarly value of our findings. We are deeply thankful for their collaboration and the essential role they have played in the progression of this study.

References

1. Li M., Lu J., Chen Z., Amine K. 30 years of lithium-ion batteries. *Advanced Materials*. 2018; 30: e1800561. https://doi.org/10.1002/adma.201800561
2. Tarascon J.-M., Armand M. Issues and challenges facing rechargeable lithium batteries. *Nature*. 2001; 414(6861): 359–367. https://doi.org/10.1038/35104644
3. Howard W.F., Spotnitz R.M. Theoretical evaluation of high-energy lithium metal phosphate cathode materials in Li-ion batteries. *Journal of Power Sources*. 2007; 165(2): 887–891. https://doi.org/10.1016/j.jpowsour.2006.12.046
4. Zheng J., Ni L., Lu Y., Qin C., Liu P., Wu T., Tang Y., Chen Y. High-performance, nanostructure $LiMnPO_4$/C composites synthesized via one-step solid state reaction. *Journal of Power Sources*. 2015; 282: 444–451. https://doi.org/10.1016/j.jpowsour.2015.02.048
5. Cao H., Wen L., Guo Z.-Q., Piao N., Hu G.-J., Wu M.-J., Li F. Application and prospects for using carbon materials to modify lithium iron phosphate materials used at low temperatures. *New Carbon Materials*. 2022; 37(1): 46–58. https://doi.org/10.1016/S1872-5805(22)60584-5
6. Han J., Yang J., Lu H., Wang J. Effect of synthesis processes on the microstructure and electrochemical properties of $LiMnPO_4$ cathode material. *Industrial & Engineering Chemistry Research*. 2022; 61(22): 7451–7463. https://doi.org/10.1021/acs.iecr.1c04639
7. Kyaw A.M.M., Panomsuwan G., Munprom R. Solid-state reaction synthesis and characterization of Mn-doped $LiFePO_4$ cathode material. *IOP Conference Series Materials Science and Engineering*. 2022; 1234(1): 12029. https://doi.org/10.1088/1757-899X/1234/1/012029
8. Julien C.M., Mauger A., Ait-Salah A., Massot M., Gendron F., Zaghib K. Nanoscopic scale studies of $LiFePO_4$ as cathode material in lithium-ion batteries for HEV application. *Ionics (Kiel)*. 2007; 13(6): 395–411. https://doi.org/10.1007/s11581-007-0149-0
9. Arinawati M., Hutama A.P., Yudha C.S., Rahmawati M., Purwanto A. Facile rheological route method for $LiFePO_4$/C cathode material production. *Open Engineering*. 2021; 11(1): 669–676. https://doi.org/10.1515/eng-2021-0068
10. Shiratsuchi T., Okada S., Doi T., Yamaki J.-I. Cathodic performance of $LiMn_{1-x}M_xPO_4$ (M = Ti, Mg and Zr) annealed in an inert atmosphere. *Electrochimica Acta*. 2009; 54(11): 3145–3151. https://doi.org/10.1016/j.electacta.2008.11.069
11. Togo M., Nakahira A. Structure refinement of Mn-substituted $LiMn_xFe_{1-x}PO_4$. *Materials Sciences and Applications*. 2018; 9(6): 542–553. https://doi.org/10.4236/msa.2018.96039

12. Li Y., Xing B., Zhang H., Wang M., Yang L., Xu G., Yang S. Simple synthesis of a hierarchical $LiMn_{0.8}Fe_{0.2}PO_4$/C cathode by investigation of iron sources for lithium-ion batteries. *RSC Advances*. 2022; 12(40): 26070–26077. https://doi.org/10.1039/d2ra04427g
13. Li Y., Xu G., Fan S., Ma J., Shi X., Long Z., Deng W., Fan W., Yang S. Synthesis of carbon-coated $LiMn_{0.8}Fe_{0.2}PO_4$ materials via an aqueous rheological phase-assisted solid-state method. *Journal of Solid State Electrochemistry*. 2020; 24(8): 821–828. https://doi.org/10.1007/s10008-020-04525-1
14. Nwachukwu I.M., Nwanya A.C., Ekwealor A.B.C., Ezema F.I. The potentials of $LiMnPO_4$ cathode material for aqueous Li-ion batteries: An investigation into solid state and green chemistry approaches. *Applied Surface Science Advances*. 2024; 19(2): 100537. https://doi.org/10.1016/j.apsadv.2023.100537
15. Oukahou S., Maymoun M., Elomrani A., Sbiaai K., Hasnaoui A. Enhancing the electrochemical performance of olivine $LiMnPO_4$ as cathode materials for Li-ion batteries by Ni–Fe codoping. *ACS Applied Energy Materials*. 2002; 5(9): 10591–10603. https://doi.org/10.1021/acsaem.2c01319
16. Kanungo S., Bhattacharjee A., Bahadursha N., Ghosh A. Comparative analysis of Li*M*PO_4 (*M* = Fe, Co, Cr, Mn, V) as cathode materials for lithium-ion battery applications – a first-principle-based theoretical approach. *Nanomaterials*. 2022; 12(19): 3266. https://doi.org/10.3390/nano12193266
17. Shu H., Wang X., Wu Q., Hu B., Yang X., Wei Q., Liang Q., Bai Y., Zhou M., Wu C., Chen M., Wang A., Jiang L. Improved electrochemical performance of $LiFePO_4$/C cathode via Ni and Mn co-doping for lithium-ion batteries, *Journal of Power Sources*. 2013; 237: 149–155. https://doi.org/10.1016/j.jpowsour.2013.03.035
18. Huynh L.T.N., Le P.P.N., Trinh V.D., Tran H.H., Tran V.M., Le M.L.P. Structure and electrochemical behavior of minor Mn-doped olivine $LiMn_xFe_{1-x}PO_4$. *Journal of Chemistry*. 2019; 2019: 5638590. https://doi.org/10.1155/2019/5638590
19. Nwachukwu I.M., Nwanya A.C., Alshoaibi A., Awada Ch., Ekwealor A.B.C., Ezema F.I. Recent progress in Mn and Fe-rich cathode materials used in Li-ion batteries. *Journal of Energy Storage*. 2022; 54: 105248. https://doi.org/10.1016/J.EST.2022.105248
20. Cao B., Wang K., Xu H., Qin Q., Yang J., Zheng W., Jin Q., Cui D. Development of magnetic sensor technologies for point-of-care testing: Fundamentals, methodologies and applications. *Sensors and Actuators A: Physical*. 2020; 312: 112130. https://doi.org/10.1016/j.sna.2020.112130
21. Gbashi K.R., Lafta S.H., Mahmood N.B. Photo-resistor applications of Bi:ZnSe nano-composition deposited on micro-glass. *Optical Materials*. 2022; 127(37): 112248. https://doi.org/10.1016/j.optmat.2022.112248
22. Gong C., Xue Z., Wen S., Ye Y., Xie X. Advanced carbon materials/olivine $LiFePO_4$ composites cathode for lithium ion batteries. *Journal of Power Sources*. 2016; 318: 93–112. https://doi.org/10.1016/j.jpowsour.2016.04.008
23. Doan T.N.L., Bakenov Z., Taniguchi I. Preparation of carbon coated $LiMnPO_4$ powders by a combination of spray pyrolysis with dry ball-milling followed by heat treatment. *Advanced Powder Technology*. 2010; 21(2): 187–196. https://doi.org/10.1016/j.apt.2009.10.016
24. Wang D., Ouyang C., Drézen T., Exnar I., Kay A., Kwon N.H., Gouerec P., Miners J.H., Wang M., Grätzel M. Improving the electrochemical activity of $LiMnPO_4$ via Mn-site substitution. *Journal of the Electrochemical Society*. 2010; 157(2): A225–A229. https://doi.org/10.1149/1.3271112
25. Hou C., Ma Y., Zhang H., Geng W., Zhang Q. Facile synthesis of $LiMn_{0.75}Fe_{0.25}PO_4$/C composite cathode material and electronic conductivity of carbon coating. *Materials Technology*. 2017; 33(1): 16–21. https://doi.org/10.1080/10667857.2017.1373488
26. Xiao J., Chernova N.A., Upreti S., Chen X., Li Z., Deng Z., Choi D., Xu W., Nie Z., Graff G.L., Liu J., Whittingham M.S., Zhang J.G. Electrochemical performances of $LiMnPO_4$ synthesized from non-stoichiometric Li/Mn ratio. *Physical Chemistry Chemical Physics*. 2011; 13(40): 18099–18106. https://doi.org/10.1039/c1cp22658d
27. Zhu J.-N., Li W.-C., Cheng F., Lu A.-H. Synthesis of $LiMnPO_4$/C with superior performance as Li-ion battery cathodes by a two-stage microwave solvothermal process. *Journal of Materials Chemistry A*. 2015; 3(26): 13920–13925. https://doi.org/10.1039/C5TA02653A
28. Lee S., Yonghyun Ch., Song H.-K., Lee K.T., Cho J. Carbon-coated single-crystal $LiMn_2O_4$ nanoparticle clusters as cathode material for high-energy and high-power lithium-ion batteries. *Angewandte Chemie International Edition*. 2012; 51(35): 8748–8752. https://doi.org/10.1002/anie.201203581
29. Zhang X., Hou M., Gedamu A., Zhu H., Wang C., Xia Y. Carbon coated nano-sized $LiMn_{0.8}Fe_{0.2}PO_4$ porous microsphere cathode material for Li-ion batteries. *Journal of Power Sources*. 2020; 448: 227438. https://doi.org/10.1016/j.jpowsour.2019.227438
30. Satyavani T.V.S.L., Kiran B.R., Kumar R.V., Kumar S.A., Naidu S.V. Effect of particle size on dc conductivity, activation energy and diffusion coefficient of lithium iron phosphate in Li-ion cells. *Engineering Science and Technology an International Journal*. 2016; 19(1): 40–44. https://doi.org/10.1016/j.jestch.2015.05.011
31. Padhi A., Nanjundaswamy K.S., Goodenough J. Phospho-olivines as positive-electrode materials for rechargeable lithium batteries. *Journal of the Electrochemical Society*. 1997; 144(4): 1188–1194. https://doi.org/10.1149/1.1837571
32. Jaafar Z.M., Jumah T.A.J., Mahmood N.B. Structural and electrical properties of high energy ball-milled $LiMnPO_4$ for solid-state batteries. *Ceramics International*. 2024; 50(1(Pt A)): 543–549. https://doi.org/10.1016/j.ceramint.2023.10.131
33. Pentimalli M., Bellusci M., Padella F. High-energy ball milling as a general tool for nanomaterials synthesis and processing. In: Aliofkhazraei M. (ed.). *Handbook of Mechanical Nanostructuring*. John Wiley & Sons, Ltd; 2015. P. 663–679. https://doi.org/10.1002/9783527674947.ch28
34. Salah N., Habib S.S., Khan Z.H., Memic A., Azam A., Alarfaj E., Zahed N., Godah S. High-energy ball milling technique for ZnO nanoparticles as antibacterial material. *International Journal of Nanomedicine*. 2011; 6: 863–869. https://doi.org/10.2147/IJN.S18267
35. Kim S.-B., Kim S.-J., Kim C.H., Kim W.S., Park K.-W. Nanostructure cathode materials prepared by high-energy ball milling method. *Materials Letters*. 2011; 65(21-22): 3313–3316. https://doi.org/10.1016/j.matlet.2011.07.023
36. Jaafar Z.M., Jumah A.-J.T., Mahmood N.B. Enhanced electrical performance of $LiMnPO_4$ by carbon coating for solid-state battery applications. *Ceramics International*. 2024; 50(13(Pt A)): 22897–22904. https://doi.org/10.1016/j.ceramint.2024.04.014
37. Jiang Y., Chen H., Mu X., He Z. Thermal decomposition of magnesium acetate in nitrogen. *Journal of Physics: Conference*

Series. 2020; 1653(1): 012057. https://doi.org/10.1088/1742-6596/1653/1/012057

38. Hatert F., Ottolini L., Wouters J., Fontan F. A structural study of the lithiophilite-sicklerite series. *Canadian Mineralogist*. 2012; 50: 843–854. https://doi.org/10.3749/canmin.50.4.843
39. Mahmood N.B., Saeed F.R., Gbashi K.R., Hamodi A., Jaffar Z.M. Structural properties of $Co_xCu_{1-x}Fe_2O_4$ solid solution, *Journal of the Mechanical Behavior of Materials*. 2021; 30(1): 220–227. https://doi.org/10.1515/jmbm-2021-0023
40. Al-Tabbakh A.A., Karatepe N., Al-Zubaidi A.B., Benchaabane A., Mahmood N.B. Crystallite size and lattice strain of lithiated spinel material for rechargeable battery by X-ray diffraction peak-broadening analysis. *International Journal of Energy Research*. 2019; 43(5): 1903–1911. https://doi.org/10.1002/er.4390
41. Priyadharsini N., Shanmugavani A., Surendran S., Senthilkumar B., Vasylechko L., Kalai S.R. Improved electrochemical performances of $LiMnPO_4$ synthesized by a hydrothermal method for Li-ion supercapatteries. *Journal of Materials Science: Materials in Electronics*. 2018; 29(36): 18553–18565. https://doi.org/10.1007/s10854-018-9972-5
42. McIntosh I.M., Nichols A.R.L., Tani K., Llewellin E.W. Accounting for the species-dependence of the 3500 cm^{-1} H_2O_t infrared molar absorptivity coefficient: Implications for hydrated volcanic glasses. *American Mineralogist*. 2017; 102(8): 1677–1689. https://doi.org/10.2138/am-2017-5952CCBY
43. Drezen T., Kwon N.-H., Bowen P., Teerlinck I., Isono M., Exnar I. Effect of particle size on $LiMnPO_4$ cathodes. *Journal of Power Sources*. 2007; 174: 949–953. https://doi.org/10.1016/j.jpowsour.2007.06.203